Analytic Wigner Distribution Function for a Split Potential Well

K. L. Jensen,[1, a)] D. A. Shiffler,[2] J. M. Riga,[2] J. R. Harris,[2] J. L. Lebowitz,[3] M. Cahay,[4] and J. J. Petillo[5]
[1)] *Code 6362, Naval Research Laboratory, Washington, DC*
[2)] *Directed Energy Directorate, Air Force Research Lab, Kirtland AFB, NM*
[3)] *Center for Mathematical Sciences Research, Rutgers University, NJ*
[4)] *Dept. of Elec. Eng. and Comp. Sci., U. Cincinnati, OH*
[5)] *Leidos, Billerica, MA*

(Dated: 16 May 2019)

The analytic Wigner function for a single well with infinite walls is extended to the configuration where half of the well is raised and the weighting of the wave functions is in accordance with a thermal Fermi-Dirac distribution. This requires a method for determining the energy eigenstates particularly near the height of the higher half-well. The methods provide a means for constructing analytic and accurate trajectories that can be used to model tunneling times. The fidelity of the trajectory model is assessed with respect to absorption of quanta related to changes within the allowable eigenstates.

PACS numbers: 29.25.Bx 73.30.+y 73.40.Gk 73.63.-b
Keywords: Quantum Tunneling, Wigner Function, electron trajectories, tunneling times

CONTENTS

I. INTRODUCTION

Physical processes in electron emission occur over a wide range of length and time scales concurrently. Intuitions developed at the macro level and falling under the guise of classical physics are problematic when extended to field emission, where electric fields $\mathcal{E} \approx 5$ GV/m induce tunneling through emission barriers with widths on the order of a nanometer from the apex of needle-like emitters, with needle and conical structures being but one contribution to field enhancement[1]. Such configurations are necessary to enable enormous field enhancement factors so as to achieve the necessary fields at the emission site while keeping fields elsewhere in the device at levels below those associated with breakdown[2] (*e.g.*, vacuum insulators can typically sustain electric fields on the order of $\mathcal{E} \approx 10$ MV/m). This entails, however, that the area from which current is being emitted at the nanosites is on the order of tens of square nanometers (or less) even if situated on conical emitters several microns in length, nanotubes, or fibers tens of micrometers in diameter.

The physics manifested at different length scales affects the utilization of field emission sources and the design of devices for which they are intended. Taking a carbon fiber as representative[3], the length scales can be categorized as (*i*) *macroscale* occurring on scales comparable to, or larger than, the emitter length; (*ii*) *mesoscale* occurring on scales comparable to the emitter tip diameter; and (*iii*) *microscale* occurring on scales much smaller than the emitter tip diameter and in principle extending to the atomic scale. Such a partitioning of effects is implicit in Schottky's Conjecture (SC), in which field enhancements occurring on different scales combine multiplicatively[4–8]. Even though microscale features contribute to emittance and the degradation of beam quality[9–12] in manners ideally addressed through particle simulation[13], the quantum mechanical nature of electron emission (particularly field and photoemission) introduces difficult complications even more pronounced if the devices are nanoscale themselves[14–16]. Even for mesoscale field emitters, their operation becomes complicated due to erosion[3], adsorption of atoms

[a)] kjensen@mailaps.org

and/or charged inclusions[17–19], backbombardment and breakdown[20–22], and other processes which dynamically change microscale surface structure or modify the emission barrier itself. The concept of field enhancement may be problematic at the atomic scale. Thus, capturing emission physics at the nanoscale in codes that predict electron beams is a pressing problem.

Similar challenges occur on short temporal scales. Transient oscillations in field and photoemission[13,23,24] can occur, analogous to virtual cathode oscillations occurring in thermionic cathodes[25], although the intuition based on "space charge limited" current needs to give way to "space charge affected" current methods[26–28] due to the interplay of emitted charge, surface field suppression, and the field-dependent emission mechanisms. The notion of electrostatic screening faces even greater difficulty when a high intensity laser focused on the emitter surface leads to changes in the surface electric field that occur over 10's of femtoseconds over nanoscale dimensions. The problems are not academic or confined to microtriodes. Fast oscillations that generate RF[29] potentially seed downstream instabilities, wanted or not, in RF tubes and particle accelerators. Fast current oscillations, as well as variation of emission quantity and direction over the emitting surface area due to surface structure at all length scales down to the atomic, will both contribute to the beam emittance in ways that vary over time (faster in the former case, slower due to erosion, adsorption, etc., in the latter case). Pushing the physics to shorter length and faster time scales is needed, and that necessitates increasingly incorporating quantum mechanical effects in simulation tools used to model electron beam devices, particularly for field emission and photoemission sources. With little modification, such conclusions also apply to nano-gap physics, heterostructures, and resonant structures on emitting surfaces[30–33], where quantum effects may be intentionally exploited.

At such time and length scales, methodologies are needed that account for tunneling time concepts[34–36]. The Wigner distribution function[37–39] may be such a candidate, as it enables a trajectory interpretation[40–42] and is uniquely well-suited for both the analysis of high speed quantum devices[43,44] and (by extension) emission phenomena. Parenthetically, it is not the only quantum trajectory method (Bohm trajectories are useful in the simulation of resonant tunneling diodes using Gaussian wave packets[45]) or quantum distribution function (the Husimi distribution is a smoothed version of the Wigner distribution function and does not have negative values, but does not correctly give charge and current densities[46]), but its straightforward evaluation from the density matrix and the ease with which multiple levels can be included via a supply function - like weighting familiar from treatments of field emission[47,48] and resonant tunneling diodes[49,50] is advantageous.

The time dependence of emission is a challenging problem[51] and poses, for example, unique difficulties in modeling ultrafast electron emission using simulation tools that must additionally account for response time[33,52], transit times in nanogaps[30], rapid modulation of intense lasers[53–55], *etc.*, in which electron migration occurring nanometers from the surface or in the nanogap is impacted by tunneling rates through and over surface barriers. In a prior work, we developed a basis for an analytical model that allowed for an exact determination of the trajectories for a model closed system[56]. In the present work, we extend the model to treat complications associated with a two region well with different depths: in such a system, the tunneling trajectories can be analyzed accurately in a systematic development that introduces emission processes in analytically tractable models.

A long term goal of such simulations is the ability to incorporate consequences of quantum mechanical tunneling processes into simulation codes that utilize electron emission models (*e.g.* particle-in-cell (PIC) codes) when the aforesaid time dependence of the emission and transport processes begin to approach those thought to characterize the tunneling process. A difficulty is that PIC codes are dependent on a particle viewpoint and so several considerations to implementing quantum models into PIC codes arise depending on how the computational version of the emission model is embodied. It is premature to assert how the trajectory viewpoint herein will be utilized in such computational models for use in codes modeling electron sources. In fact, doing so may result in lengthy calculations for each emission site or surface patch of a mesoscale area. If that occurs, then use may be made of techniques developed previously in the delayed emission models[52]: pre-calculation of emission processes for which the results populate tables for quick access, assuming the storage needs are tractable. If the physics of the temporal delays associated with the processes span several simulation time steps, then an approach where data for each emission site is accumulated and stored and then used to spawn particles at each time step, the emission process may then be integrated along in time as the generation of a charge bunch or pulse evolves. Simulations that serve to capture microscopic emission processes that happen on fast time scales will certainly be too fine-scaled to use directly for macroscopic-level simulations, and possibly even for mesoscale simulations. In this case, the microscopic effects can be captured and re-introduced macro- or mesoscopically in component simulations using the methods reported in Ref. 52.

The organization of the remainder of the present work is undertaken in the following steps: the method to evaluate the Wigner function is briefly recounted; the energy eigenstates are identified and a means to evaluate them demonstrated; the density for wave functions weighted by a thermal Fermi-Dirac distribution are evaluated; an analytic Wigner Distribution Function for the split level potential is constructed; the effects of a split well on the resultant Wigner trajectories is shown; and lastly, the consequences of exciting a single level (such as in photoabsorption) on the resultant trajectories are examined.

II. WAVE FUNCTIONS AND DENSITY

A. Dimensionless Formulation

For the split-well model, the wave functions $\psi_k(x) = \langle k|x\rangle$ are solutions to Schrödinger's equation given by

$$\left[-\frac{\partial^2}{\partial x^2} + k_o^2\ \Theta(x) - k^2\right]\psi_k(x) = 0 \tag{1}$$

where $\Theta(x)$ is the Heaviside step function (0 for $x < 1$ and 1 otherwise), $k = \sqrt{2m_nE}/\hbar$, $k_o = \sqrt{2m_nV_o}/\hbar$ with V_o the height of the step, and m_n the effective mass (m without a subscript is taken to be the rest mass such that $mc^2 = 0.511$ MeV), and $r = 1$ for an electron in free space. Infinite walls at $x = \pm L/2$ entail the boundary conditions $\psi_k(\pm L/2) = 0$.

Working in dimensionless coordinates eases computation and brings out subtle features in the discussion. Therefore, below, dimensioned coordinates will be designated with a tilde and dimensionless coordinates without, and so $\tilde{x} = xL/2$, $\tilde{k} = 2\pi k/L$, with $k = n + s$ being the sum of an integer n with a remainder $0 \le s < 1$ for split wells where $k_o \neq 0$. As a result, the product of the wave number with position $\tilde{k}\tilde{x}$, is now given by $\pi kx = \pi(n + s)x$, forms used interchangeably depending on the needs of the discussion. The boundaries of the well region occur at $x = \pm 1$. The separating out of the integer part of k is essential to obtain various representations below; computational demands are then eased by having k_o and k_F only take on integer values, that is $k_o \to N$ and $k_F \to n_f$, but such a restriction does not affect the generality of the results.

B. Eigenstate Determination

The energy levels E_j are discrete. The k_j levels associated with them are indexed sequentially by j so that $k \to k_j = n_j + s_j < k_{j+1}$. When speaking of a particular level, it is useful to suppress the index on n and s, but its presence is implied. Two limiting cases are important:

- Half-well: a well exists only on the $x < 0$ side, so that $V_o = \infty$ (corresponding to $N \to \infty$), for which $k_j = n_j = j$ and $s_j = 0$ (as found previously[56] and a consequence of elementary arguments[57]). The energy levels are $E_j(\text{half}) = 2\pi^2\hbar^2j^2/m_nL^2$.
- Full-well: a well exists from $-1 < x < 1$, so that $V_o = 0$ (corresponding to $N = 0$), for which $k_j = j/2$, so that $n_j = j/2$ and $s_j = 0$ for j even and $n_j = (j-1)/2$ and $s_j = 1/2$ for j odd. The energy levels are $E_j(\text{full}) = \pi^2\hbar^2j^2/2m_nL^2$.

The energy levels are indexed by j. It is notationally preferable to recast the wave function $\psi_k(x)$ as either $\langle n + s|x\rangle$ or $\langle k_j|x\rangle$. Examples of $\langle n + s|x\rangle$ for $k_o \equiv N = 5$ are shown in Figure 1.

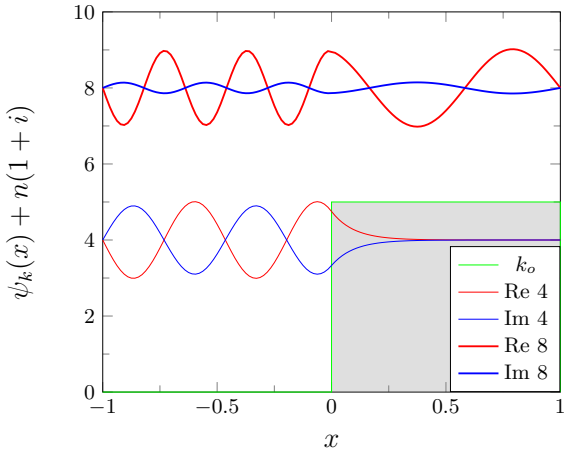

FIG. 1. Wave functions $\psi_k(x) \to \langle n + s|x\rangle$ for $k_o = 5$ in dimensionless units for the 4^{th} and 8^{th} energy levels showing decay for $n+s < k_o$ and oscillation for $n+s > k_o$ in the raised split-well region (gray). The green line labeled k_o represents the profile of the split well configuration.

Determination of the eigenstates for when the right side of the split well is finite in height (N finite and non-zero) entails non-zero values of s that are determined using standard methods[57] that are recast in the dimensionless framework. Introduce the wave number $\sqrt{k_o^2 - k^2} \to q = \left[N^2 - (n+s)^2\right]^{1/2}$ when $N > n + s$, and let $q \to ip$ when $N < n + s$ such that q and p are positive, real numbers. The boundary conditions are such that at $x = \pm 1$ the wave function vanishes, and so

$$\langle k_j|x\rangle = \begin{cases} 2Aie^{-i\pi s}\sin\{\pi[(n+s)x+s]\} & (x \le 0) \\ 2Bie^{-i\pi q}\sin[\pi q(1-x)]] & (x > 0) \end{cases} \tag{2}$$

where $iq \to -p$ when $n + s \le N$. It is seen that usage of q occurs with $N > n + s$ and p with $N < n + s$, and so these regimes are referred to q and p, respectively. Next, the continuity of the wave function and its first derivative constitute two relations, one of which determines the values of k_j and the other of which determines B in terms of A. They result in the relations

$$0 = \frac{\tan(\pi q)}{q} + \frac{\tan(\pi s)}{n+s} \tag{3}$$

$$\frac{B}{A} = -\frac{e^{i\pi(2q-s)}}{q}\left[(n+s)\cos(\pi s) + iq\sin(\pi s)\right] \tag{4}$$

for the q regime, and $q \to ip$ for the p regime. Eq. (3) reproduces the full and half well energy levels in the $N \to 0$ and $N \to \infty$ limits. For finite non-zero N, referred to henceforth as "split-well", $k_j = n_j + s_j$ has to be found numerically, the method here being to define the absolute value of the right hand side of Eq. (4) as $F(s)$ and searching for the value of s for which $F(s) = 0$ for a

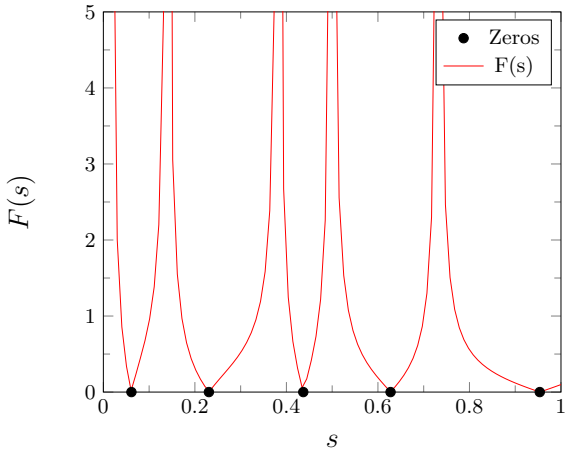

FIG. 2. Zeros of Eq. (3) for $n = N = 8$. The number of zeros in this regime goes approximately as $\sqrt{2N+1}$.

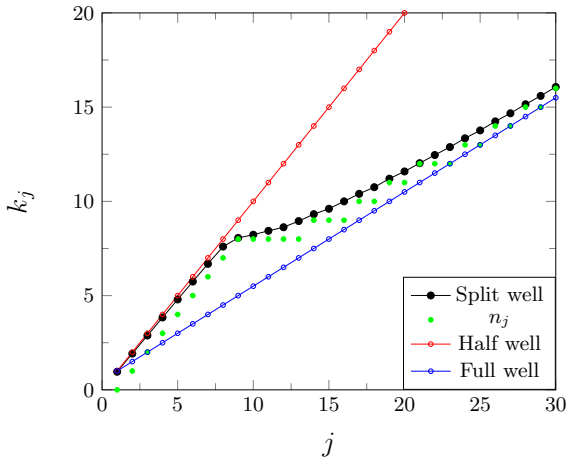

FIG. 3. Eigenvalues $k_j = n_j + s_j$ for $N = 8$ (black dots), compared to the half-well ($N \to \infty$, red) corresponding to $k_j = j/2$, and the full-well ($N \to 0$, blue) corresponding to $k_j = j$. "n_j" shows the k_j rounded down to the nearest integer (that is, without s_j) for the split well condition.

given value of $n - N$ that is located between the singular points defined by $F(s) \to \infty$, although that method fails when q is integer for which those points must be inserted separately. When $n - N < 0$, only one zero exists per n. When $n - N \gg 1$, then two zeros exist for each value of n. However, when $n = N$, the number of zeros goes as approximately $\sqrt{2N+1}$, as shown in Figure 2. As a result, and perhaps unexpectedly, a number of energy levels *are found to cluster* near $n = N$, in which the n_j are equal for a number of j even though the s_j differ, as seen in the representative case for $N = 8$ in Figure 3, where five k_j occur having the same $n_j = 8$ (shown as green dots).

C. Density

In contrast to the uniform spacing of the k-levels for full ($N = 0$) and half ($N \to \infty$) well conditions for which $k_{j+1} - k_j = \Delta$ is constant, the non-uniform spacing for split well conditions must be accounted for in the evaluation of density using the density matrix. To prepare, the transition from the zero temperature continuum evaluation of the density using the supply function over to the discrete form follows standard methods in approximating integrations by summations, the dimensioned integral in question being

$$\rho = \frac{1}{\pi}\int_0^\infty f(\tilde{k})d\tilde{k} \tag{5}$$

where a factor of 2 for electron spin is implicit. In the zero temperature limit where $f(\tilde{k}) = (\tilde{k}_F^2 - \tilde{k}^2)/2\pi$, then $\rho \to \rho_o = \tilde{k}_F^3/3\pi^2$, a standard result[58,59], where $\tilde{k}_F$ is defined from the chemical potential μ by $\sqrt{2m_n\mu}/\hbar = \tilde{k}_F$. For uniformly spaced k_j characteristic of half-wells ($N \to \infty$), for which $\Delta = k_{j+1} - k_j = 2\pi/L$, the discrete formulation in the dimensionless x and k notation are obtained by introducing

$$\alpha = \frac{2\pi^2\hbar^2}{mk_BTL^2}; \quad \gamma = \frac{1}{\hbar\alpha L^2} \tag{6}$$

as well as $\tilde{k}_F = 2\pi n_f/L$, and so $f(\tilde{k})d\tilde{k} = 4\pi^2(n_f^2 - j^2)/L^3$ in the zero temperature limit. The discrete form of Eq. (5) then becomes

$$\frac{\rho_n}{\rho_o} = \frac{3}{4n_f}\left[1 + 2\sum_{j=1}^{n_f}\left(1 - \frac{j^2}{n_f^2}\right)\right] = 1 - \frac{1}{4n_f^2} \tag{7}$$

As with $k_o = N$, restricting n_f to take only integer values is convenient. The form of Eq. (7) is equivalent to $\rho_n = (\tilde{k}_F^3/3\pi^2)\left[1 - (\pi/\tilde{k}_F L)^2\right]$ in dimensioned terms.

When the spacing between the k_j becomes non-uniform, and when temperature is non-zero, then Eq. (7) is amended by the introduction of Δ_j and f_j respectively. The spacing between the levels is now designated by Δ_j and defined as the separation between $k_{j\pm1/2}$. It is given by

$$\Delta_j = \frac{1}{2}\left(k_{j+1} - k_{j-1}\right) \tag{8}$$

The weighting factor f_j is now modeled after the temperature dependent supply function $f(k)$, found by integrating the Fermi Dirac distribution $f_{FD}(E) = 1/\{1 + \exp[(\mu - E)/k_BT]\}$ with $E = (\hbar^2/2m_n)(\tilde{k}_\rho^2 + \tilde{k}_z^2)$ over the transverse energy components $2\pi\tilde{k}_\rho d\tilde{k}_\rho$. It can be represented as

$$f_j = \gamma \ln\left\{1 + \exp\left[\alpha\left(n_f^2 - (n_j + s_j)^2\right)\right]\right\} \tag{9}$$

Classical behavior results when the spacing between the energy levels becomes small and when the Fermi

Dirac distribution $f_{FD}(E)$ transitions to the Maxwell-Boltzmann distribution $f_{MB}(E)$. The former is a consequence of L becoming large, and the latter is often associated with a rise in temperature T (for which $\mu(T)$ becomes negative such that the density does not change). However, since L and T appear only in the combination mTL^2 in α, it is convenient to hold L fixed at a representative value (*e.g.*, $L = 50$ nm), take $m_n \to m$ as the electron rest mass, and only speak of changes in T: it is not intended to obscure the onset of quantum behavior in the limits of low temperature T *or* small values of L.

When summing over the states, Eq. (7) then becomes

$$\rho = \sum_{j=1}^{\infty} f_j \Delta_j \left| \langle n_j + s_j | x \rangle \right|^2 \tag{10}$$

where the absence of a $j = 0$ state is apparent (the quantum mechanical ground state energy is non-zero). Finally, the normalization A must be generalized from the half-well case[56], and account for both the dimensionless form and the range of x. Requiring that the wave function be normalized over the $-1 \leq x \leq 1$ region of the split well $\langle n + s | x \rangle$ results in

$$A = \frac{1}{(\mathcal{N}_- + \mathcal{N}_+)^{1/2}} \tag{11}$$

$$\mathcal{N}_- = 2 - \frac{\sin(2\pi s)}{\pi(n+s)} \tag{12}$$

where the $(\pm)$ subscript refers to the negative and positive regions over which $|\langle n + s | x \rangle|^2$ is integrated. Clearly, when $s = 0$, the half-well result is recovered for $\mathcal{N}_-$. $\mathcal{N}_+$ depends on the relation of n to N, and is

$$\begin{aligned} \mathcal{N}_+(n < N) &= \frac{(n+s)^2[\sinh(2\pi p) - 2\pi p]\cos^2(\pi s)}{\pi p^3 \cosh^2(\pi p)} \\ \mathcal{N}_+(n > N) &= \frac{[2\pi q - \sin(2\pi q)][N^2\cos^2(\pi s) + q^2]}{\pi q^3} \end{aligned} \tag{13}$$

where the j subscripts on n, s, q and p are suppressed for clarity. Lastly, in the exceptional case that q is an integer (*e.g.* for $N = 20$, $n - N = 4$, and $s = 1$, then $q = 15$), Eq. (11) reduces to

$$A = \frac{q}{\sqrt{4q^2 + 2N^2}} \tag{14}$$

The density as evaluated using Eq. (10) is shown in Figure 4 for various step heights governed by $k_o = N$ for $n_f = 6$. Observe that oscillations are mitigated when the barrier *and* temperature are high. Observe also that the density increases with temperature as a consequence of k_F being held fixed (in contrast, for a constant density, the chemical potential $\mu(T)$ is temperature dependent, decreasing as T increases for Fermi Dirac statistics when the density is held constant[58,59]).

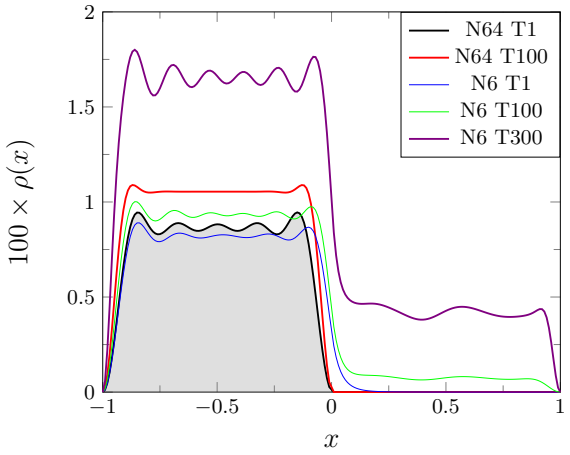

FIG. 4. Density evaluated via Eq. (10) for step height governed by N and temperature T (Kelvin) for $n_f = 6$. The half-well solution (gray fill) is approximated by a very high well step ($N = 64$); the low split-well solution is for $N = n_f$.

III. HALF-WELL WIGNER FUNCTION

The half-well configuration restricts a well of width $L/2$ to the $x < 0$ region but is otherwise analogous to the full-well centered at the origin[56]. The changes as a consequence of doing so are briefly recounted.

A. Pure State

The Wigner function $f(\tilde{x}, \tilde{k})$ is defined by

$$\begin{aligned} f(\tilde{x}, \tilde{k}) &= \frac{1}{\pi} \int_{-\infty}^{\infty} e^{2i\tilde{k}\tilde{y}} \langle \tilde{x} - \tilde{y} | \hat{\rho} | x + \tilde{y} \rangle \, d\tilde{y} \\ &= \frac{2}{\pi} \int_{0}^{\infty} \Re \left\{ e^{2i\tilde{k}\tilde{y}} \langle \tilde{x} - \tilde{y} | \hat{\rho} | x + \tilde{y} \rangle \, d\tilde{y} \right\} \end{aligned} \tag{15}$$

where $\hat{\rho}$ is the density matrix and where the second form is of greater utility here. Switching to the dimensionless units of Eq. (2) for a pure state $\hat{\rho} = |n\rangle \langle n|$ because the states are characterized by $s = 0$, then for the half-well ($N \to \infty$) and so

$$\psi_n(x) = \langle n | x \rangle = 2Ai \sin(2\pi n x) \tag{16}$$

where $A = 1/\sqrt{2}$ from Eq. (11). The infinite walls at $x = -1$ and $x = 0$ constrain the integration region in y, as a consequence of the wave function $\psi_n(x)$ vanishing for $x < -1$ and $x > 0$, and so $\psi_n(x + y) = 0$ for $y > 1 - |x|$. A similar relation holds for $\psi_n(x - y)$. Because $\langle x - y | \hat{\rho} | x + y \rangle$ is an even function in y for wave functions given by Eq. (16), the integral may be re-expressed as an integration only over positive y, and so the dimensionless form becomes

$$f(x, k) = 2A^2 \int_0^{y_{max}} \cos(2\pi k y) \, \sin\theta_n^+ \, \sin\theta_n^- \, dy \tag{17}$$

where $\theta_n^{\pm} = 2\pi n(x \pm y + 1)$ and

$$y_{max} = \begin{cases} 1 - |x| & (x \leqslant -1/2) \\ |x| & (x > -1/2) \end{cases} \tag{18}$$

The trigonometric functions are straightforward to integrate, and it is found (compare Refs. 38 and 56 for wells placed symmetrically about the origin, as opposed to here where the well is entirely on the $x < 0$ side)

$$\begin{aligned} f_n^{>}(x,k) = \frac{x}{4} \{ & -\operatorname{sinc}[2\pi(k+n)x] \\ & -\operatorname{sinc}[2\pi(k-n)x] \\ & +2\cos[2\pi n(1+x)]\operatorname{sinc}(2\pi kx)\} \end{aligned} \tag{19}$$

$$\begin{aligned} f_n^{<}(x,k) = \frac{1+x}{4} \{ & \operatorname{sinc}[2\pi(k+n)(1+x)] \\ & +\operatorname{sinc}[2\pi(k-n)(1+x)] \\ & -2\cos(2\pi nx)\operatorname{sinc}[2\pi k(1+x)]\} \end{aligned} \tag{20}$$

where the ">" and "<" superscripts on f_n denote $(x > -1/2)$ and $(x < -1/2)$, respectively, and where $\operatorname{sinc}\theta = (\sin\theta)/\theta$. For $n = 1$, the familiar ground state (*e.g.*, Figure (3) of Ref. [38]; see Figure (4) for a higher state) is recovered. For exploring the relationship to trajectories associated with contour lines[56], considering the behavior for higher states, such as $n = 3$ shown in Figure 5, is more profitable.

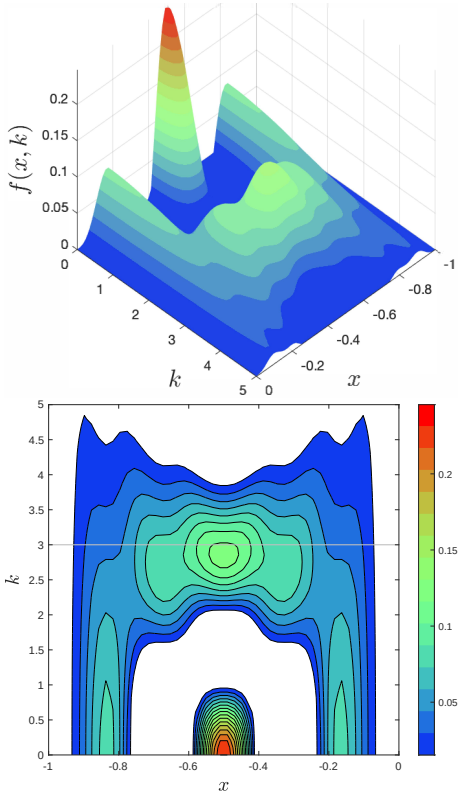

FIG. 5. (top) Half-well pure state Wigner function for $n = 3$. Negative regions are not shown to aid the visibility of the positive regions. (bottom) top-down view of the positive values of $f(x,k)$ for which the contour lines corresponding to trajectories are in black, and the classical trajectory with a velocity $v = 2\pi\hbar n/m_n L$ is the horizontal gray line.

B. Mixed State

The zero-temperature mixed state $\hat{\rho}$ of our prior treatment[56] can now be generalized to arbitrary temperatures, where $\hat{\rho}$ can be inferred from Eq. (10) to be

$$\hat{\rho} = \sum_{j=1}^{\infty} f_j \Delta_j \left|n_j\right\rangle \left\langle n_j\right| \tag{21}$$

for the half-well configuration. For the half-well, this entails setting Δ_j to a constant and summing the $f_n(x,k)$ of Eqs. (19) and (20) weighted by f_j from Eq. (9) with $s_j = 0$. The $T = 0$ K case for $n_f = 6$ is shown in Figure 6. Using this configuration as a baseline, the trajectories for increasing temperature ($T = 1, 10, 100$ K) are shown in Figure 7. As the temperature increases, more states (more non-negligible f_j in Eq. (21)) contribute and cause the undulations apparent in $f(x,k)$ to become muted and the trajectories to more closely match their classical analogues. This is in keeping with the expectation that higher temperatures (or wells of greater width) approach classical behavior through a reduction in the spacing of energy levels and the dampening of interference effects. Notably, this behavior is evident in the absence of scattering, insofar as scattering suppresses oscillations associated with abrupt barriers.

More relevant to the present study, however, is the close similarity of these analytic solutions to Wigner functions for open boundary conditions as considered in the simulation of resonant tunneling diodes[40,50] and other quantum electronic devices, for which the Review by Weinbub and Ferry[60], and references therein, cover many instances. The investigation of tunneling is now possible by finding the analytic solution to $f(x,k)$ for finite temperature and finite split-well conditions (finite non-zero N).

IV. SPLIT-WELL WIGNER FUNCTION

A. Wave Function

Two modifications to the analysis as a consequence of Eq. (2) occur. First, the states k_j are no longer integer as for the half-well, but acquire an additional term s so that $k_j = n_j + s_j$, where n_j is integer and $s_j < 1$ and

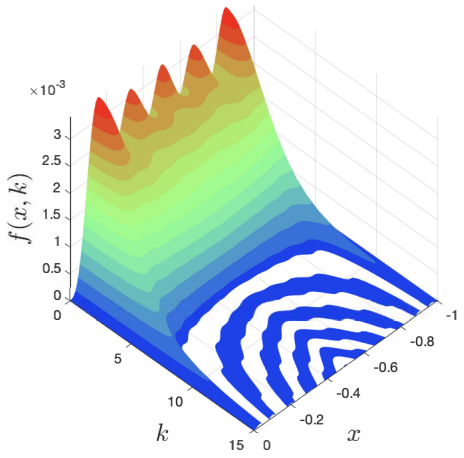

FIG. 6. Half-well mixed state Wigner function for $n_f = 6$ at $T = 0$ K. Negative regions are not shown for visual clarity, and appear as blank.

specified by Eq. (3). For this collection of eigenstates, Eq. (2) is generalized to

$$p = N^2 - (n_j + s_j)^2 \qquad (k_j < k_o) \tag{22}$$

$$q = (n_j + s_j)^2 - N^2 \qquad (k_j > k_o) \tag{23}$$

and defined such that both q and p are always positive and real, entailing that when k_j passes from above $k_o = N$ to below it, then $q \to ip$. For convenience, the j-subscript dependence of p and q is understood but not explicitly shown. Second, the spatial integration of the Wigner function now extends into the $x > 0$ region as a consequence of the generalized pure state wave function now given by $\hat{\rho} \to |k_j\rangle \langle k_j|$ where

$$\begin{aligned} \langle x|k_j\rangle =& iAe^{-i\pi k_j} \sin[\pi k_j(1+x)]\ \Pi(-x) \\ &+ Be^{-\pi p} \sinh[\pi p(1-x)]\ \Pi(x) \\ \equiv& \langle x|A\rangle + \langle x|B\rangle \end{aligned} \tag{24}$$

where $p \to -iq$ when $k_j > N$, and where $\Pi(\pm x) = \Theta(\pm x)\Theta(1 \mp x)$ is a product of Heaviside Step functions. Because of the combination of the Π-functions and y_{max} of Eq. (18), four integration domains result. Using the suggestive notation of $\{AA\} = \Re\left\{e^{2i\pi k y} \langle x - y|A\rangle \langle A|x + y\rangle\right\}$ and similarly for $\{AB\}$ and $\{BB\}$, then the integrands associated with $\{AA\}, \{AB\}, \{AB\}$, and $\{BB\}$ can be specified, and their integrals evaluated. The domain will dictate the subscript on $f(x, k)$. Functions that are involved in the resulting integrals are

$$\mathcal{R}(z, a, b) \equiv \frac{z\left[a\cos(b)\sinh(a) + b\cosh(a)\sin(b)\right]}{a^2 + b^2} \tag{25}$$

$$\begin{aligned} \mathcal{S}(z, \alpha, a, \beta, b) \equiv\ & \frac{\beta\ \cos(\alpha z + a)\ \cosh(\beta z + b)}{\alpha^2 + \beta^2} \\ & \frac{\alpha\ \sin(\alpha z + a)\ \sinh(\beta z + b)}{\alpha^2 + \beta^2} \end{aligned} \tag{26}$$

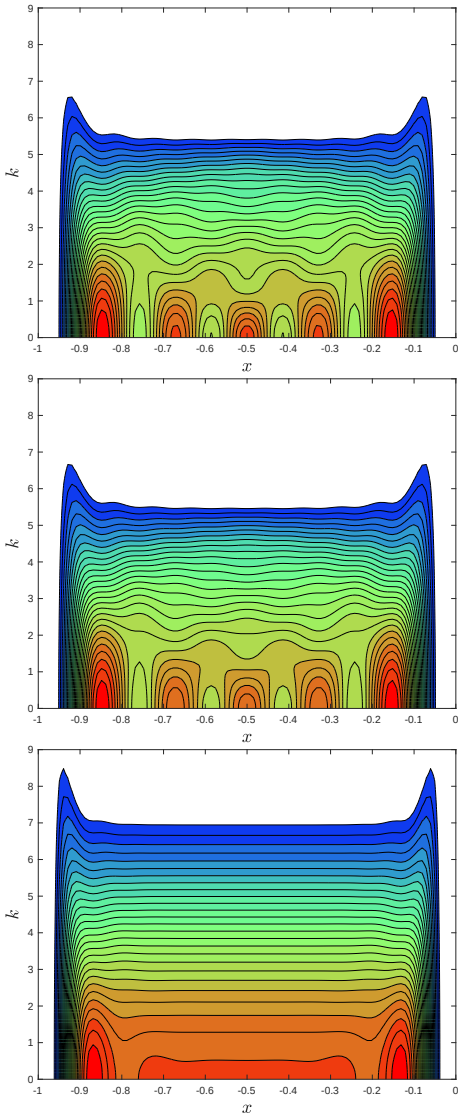

FIG. 7. Half-well mixed state Wigner function trajectories for $n_f = 6$ and increasing temperatures: (*top*) $T = 1$ K; (*middle*) $T = 10$ K; (*bottom*) $T = 100$ K. The $T = 1$ K case is indistinguishable from $T = 0$ K case. Negative regions are not shown for visual clarity, and appear as blank. Color of regions between trajectories correspond to color map of Figure 6.

$$\begin{aligned} \mathcal{T}(z, \alpha, a) \equiv\ & (1 - 2z)\cos\left(\frac{\alpha}{2} + a\right) \times \\ & \operatorname{sinc}\left[\frac{\alpha}{2}(1 - 2z)\right] \end{aligned} \tag{27}$$

where the dummy arguments (z, α, a, β, b) are combinations of (x, k, k_j, q, p) and vary in their definitions according to the domain and regime under discussion. Recall that $k_j = n_j + s_j$ for compactness. Lastly, the coefficient B is complex, and so define the phase angle φ by

$$B = |B|e^{i\varphi} \equiv B_o e^{i\varphi} \tag{28}$$

B. Integral Evaluations

1. AA Domain

When the components associated with Eq. (24) are inserted into Eq. (15), then the Wigner function in the AA domain where $(-1 \le x < -1/2)$ results in an integral of the form

$$f_{AA}(x,k) = \frac{A^2}{\pi}\int_0^{1-|x|} I_{AA}\, dy \equiv \frac{A^2}{\pi} M'_{AA} \tag{29}$$

where the M-notation is introduced, and I_{AA} is

$$\begin{aligned} I_{AA} =& \cos(2\pi k y)\times \\ & \sin[\pi k_j(x+y+1)]\ \sin[\pi k_j(x-y+1)] \end{aligned} \tag{30}$$

The integration is analytic and results in

$$\begin{aligned} M'_{AA} =\ & x' \left[\mathrm{sinc}(\phi'_+) + \mathrm{sinc}(\phi'_-)\right. \\ & \left. -2\cos(2\pi k_j x')\,\mathrm{sinc}(2\pi k x')\right] \end{aligned} \tag{31}$$

where $x' \equiv 1 + x = 1 - |x|$ and $\phi'_\pm = 2\pi(k \pm k_j)x'$, and is the cause of the prime on M'_{AA} in Eq. (29).

2. AB Domain

The Wigner function in the AB domain where $(-1/2 \le x < 0)$ results in integrals of the form

$$f^r_{AB}(x,k) = \frac{A^2}{\pi}\int_0^{|x|} I_{AA} dy + \frac{AB_o}{\pi}\int_{|x|}^{1-|x|} I^r_{AB} dy \tag{32}$$

where r-superscript on I^r_{AB} designates either q or p. The first and second integrals are designated M_{AA} and M^r_{AB}, respectively. I_{AA} is unchanged from Eq. (30). The I^r_{AB} integrands are

$$\begin{aligned} I^q_{AB} =& \cos[\varphi + \pi(2ky + k_j - q)]\times \\ & \sin[\pi k_j(x-y+1)]\ \sin[\pi q(-x-y+1)] \end{aligned} \tag{33}$$

$$\begin{aligned} I^p_{AB} =& \sin[\varphi + \pi(2ky + k_j)]\ e^{-\pi p}\times \\ & \sin[\pi k_j(x-y+1)]\sinh[\pi p(-x-y+1)] \end{aligned} \tag{34}$$

The first integral is

$$\begin{aligned} M_{AA} =& x\left[\mathrm{sinc}(\phi_+) + \mathrm{sinc}(\phi_-)\right. \\ & \left. -2\cos[2\pi k_j(1+x)]\,\mathrm{sinc}(2\pi k x)\right] \end{aligned} \tag{35}$$

where $\phi_\pm = 2\pi(k \pm k)x$. The second integral depends on regime. When $r \to p$,

$$\begin{aligned} M^p_{AB} = 2e^{-\pi p}\{ & -\mathcal{S}(1+x,\alpha,a,-\gamma,c) \\ & +\mathcal{S}(-x,\alpha,a,-\gamma,c) \\ & +\mathcal{S}(1+x,\beta,b-\gamma,c) \\ & -\mathcal{S}(-x,\beta,b,-\gamma,c)\} \end{aligned} \tag{36}$$

where the arguments are

$$\begin{aligned} &\alpha = \pi(2k - k_j), && \beta = \pi(2k + k_j), && \gamma = \pi p \\ &a = \varphi + \pi k_j(x+2), && b = \varphi - \pi k_j x, && c = \pi p(1-x) \end{aligned}$$

Conversely, when $r \to q$,

$$\begin{aligned} M^q_{AB} =& \mathcal{T}(-x,\beta+\gamma,b+c) + \mathcal{T}(-x,\beta-\gamma,b-c) \\ & -\mathcal{T}(-x,\alpha+\gamma,a+c) - \mathcal{T}(-x,\alpha-\gamma,a-c) \end{aligned} \tag{37}$$

where the arguments are now

$$\begin{aligned} &\alpha = -\pi(k_j + q), && \beta = -\pi(k_j - q), && \gamma = 2\pi k \\ &a = -\beta x - \alpha, && b = -\alpha x - \beta, && c = \varphi - \beta \end{aligned}$$

3. BA Domain

The Wigner function in the BA domain where $(0 \le x < 1/2)$ results in integrals of the form

$$f^r_{BA}(x,k) = \frac{B_o^2}{\pi}\int_0^x I^r_{BB} dy + \frac{AB_o}{\pi}\int_x^{1-x} I^r_{BA} dy \tag{38}$$

The I^r_{BB} integrands are

$$\begin{aligned} I^p_{BB} =& 2e^{-2\pi p}\cos(2\pi k y)\times \\ & \sinh[\pi p(-x+y+1)]\ \sin[\pi p(-x-y+1)] \end{aligned} \tag{39}$$

$$\begin{aligned} I^q_{BB} =& 2\cos(2\pi k y)\times \\ & \sin[\pi q(-x+y+1)]\ \sin[\pi q(-x-y+1)] \end{aligned} \tag{40}$$

whereas the I^r_{BA} integrands are

$$\begin{aligned} I^p_{BA} =& 2e^{-\pi p}\sin[\varphi + \pi(2ky + k_j)]\times \\ & \sin[\pi k_j(x-y+1)]\ \sinh[\pi p(-x-y+1)] \end{aligned} \tag{41}$$

$$\begin{aligned} I^q_{BA} =& 2\cos[\varphi + \pi(2ky + k_j - q)]\times \\ & \sin[\pi k_j(x-y+1)]\ \sin[\pi q(-x-y+1)] \end{aligned} \tag{42}$$

The BB integral is considered first. In the p-regime, it is

$$M^p_{BB} = 2e^{-2\pi p}\left[-\mathcal{R}(x,a,b) + x\cosh(c)\,\mathrm{sinc}(b)\right] \tag{43}$$

where the arguments are

$$a = 2\pi p x \quad b = 2\pi k x \quad c = 2\pi p(1-x)$$

In the q-regime, it is

$$M^q_{BB} = x\left[\mathrm{sinc}(\alpha) + \mathrm{sinc}(\beta) - 2\cos(\delta)\,\mathrm{sinc}(\gamma)\right] \tag{44}$$

where the arguments are now

$$\begin{aligned} &\alpha = 2\pi(k+q)x && \beta = 2\pi(k-q)x \\ &\gamma = 2\pi k x && \delta = 2\pi q(1-x) \end{aligned}$$

The BA integral is considered next. In the p-regime it is

$$\begin{aligned} M^p_{BA} = 2e^{-\pi p}\{ & \mathcal{S}(x,\alpha,a,-\gamma,c) \\ & -\mathcal{S}(1-x,\alpha,a,-\gamma,c) \\ & -\mathcal{S}(x,\beta,b,-\gamma,c) \\ & +\mathcal{S}(1-x,\beta,b,-\gamma,c)\} \end{aligned} \tag{45}$$

where the arguments are the same as those for Eq. (36), but for clarity are

$$\begin{array}{lll} \alpha = \pi(2k - k_j) & \beta = \pi(2k + k_j) & \gamma = \pi p \\ a = \varphi + \pi k_j(x + 2) & b = \varphi - \pi k_j x & c = \pi p(1 - x) \end{array}$$

In the q-regime the integral is

$$\begin{aligned} M^q_{BA} =& \mathcal{T}(x, \alpha + \gamma, a + c) + \mathcal{T}(x, \alpha - \gamma, a - c) \\ & - \mathcal{T}(x, \beta + \gamma, b + c) - \mathcal{T}(x, \beta - \gamma, b - c) \end{aligned} \tag{46}$$

where the arguments are now

$$\begin{array}{lll} \alpha = \pi(q - k_j), & \beta = -\pi(q + k_j), & \gamma = 2\pi k \\ a = -\beta x - \alpha, & b = -\alpha x - \beta, & c = \varphi - \alpha \end{array}$$

4. BB Domain

Finally, the Wigner function in the BB domain where $(1/2 \le x \le 1)$ results in the integrands

$$\begin{aligned} I^p_{BB} =& 2\cos(2\pi k y) \times \\ & \sinh[\pi p(-x + y + 1)] \sinh[\pi p(-x - y + 1)] \end{aligned} \tag{47}$$

$$\begin{aligned} I^q_{BB} =& 2\cos(2\pi k y) \times \\ & \sin[\pi q(-x + y + 1)] \sin[\pi q(-x - y + 1)] \end{aligned} \tag{48}$$

The associated integrals are, for the p-regime

$$\begin{aligned} M^p_{BB} =& 2e^{-2\pi p} \frac{(1 - x)}{x} \times \\ & [-\mathcal{R}(x, a, b) + x \cosh(a) \operatorname{sinc}(b)] \end{aligned} \tag{49}$$

where $(x' = 1 - x)$ and the arguments are

$$a = 2\pi p x' \quad b = 2\pi k x'$$

whereas the integral for the q-regime is

$$M^q_{BB} = x' \left[\operatorname{sinc}(a) + \operatorname{sinc}(b) - 2\cos(d) \operatorname{sinc}(c)\right] \tag{50}$$

where $(x' = 1 - x)$ and the arguments are now

$$\begin{array}{ll} a = 2\pi(k + q)x', & b = 2\pi(k - q) \\ c = 2\pi k x', & d = 2\pi q x' \end{array}$$

C. Tunneling Trajectories

A large value of N approximates the half-well configuration: as an example, for $N = 64$ and $T = 1$, $f(x, k)$ for the split-well is visually indistinguishable from Figure 6. In the same way, the density $\rho(x) = \pi^{-1} \int f(x, k) dk$ (analogous to Eq. (5)) is indistinguishable from the $N64T1$ line of Figure 4. The corresponding trajectory representation, however, now includes the $x > 0$ region, and so is shown in Figure 8 for 16 uniformly spaced contours starting at 0.0625, where $f(x, k)$ has been normalized to the maximum of $f_o(x, k)$. As N declines, the

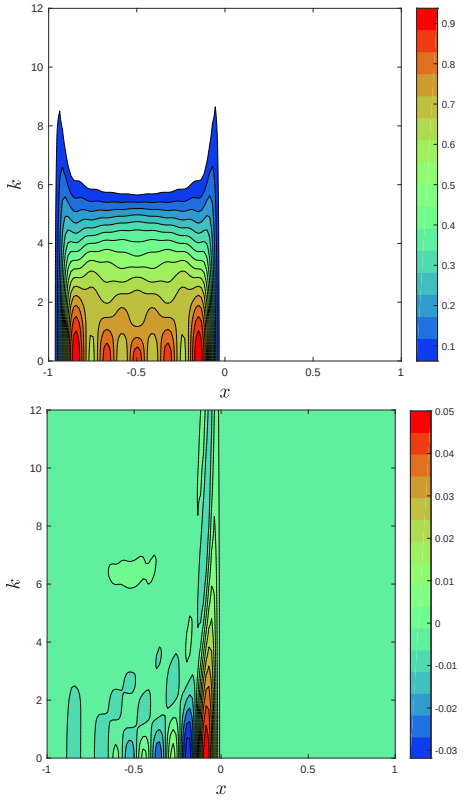

FIG. 8. Split-well mixed state Wigner function trajectories for $n_f = 6$, $N = 64$, and $T = 1$ K. (*top*) $f(x, k)$: compare to Figure 7(a). (*bottom*) $\Delta f(x, k) = f(x, k) - f_o(x, k)$, showing the small changes that occur as a consequence of large but finite N, with negative regions shown. Normalization is to the maximum of $f_o(x, k)$.

figure does not visually change until N approaches n_f, and even then, the differences can be hard to discern. It is therefore useful to define the state $f_o(x, k)$ as the $N \to \infty$ state for a given n_f and T and then to examine $f(x, k) - f_o(x, k) \equiv \Delta f(x, k)$ so as to emphasize departures from the half-well configuration of Figure 7 even though the magnitude of the differences is small; the color bar is with respect to the maximum of $f_o(x, k)$ for both top and bottom figures, as will also be done below. Consequently, for smaller N, the onset of tunneling trajectory behavior will become readily apparent. In showing the Wigner function, only the $k \ge 0$ region is needed for visualization because for a closed system, $f(x, -k) = f(x, k)$, that is, the Wigner function is symmetric about the k-axis.

The exercise is now repeated for $N = 9$ for both $T = 1$ K and $T = 300$ K to show the emergent tunneling behavior apparent near the origin for small k. The results are shown in Figure 9 where the maximum k shown has been increased to 12. Visible in the difference comparison is the depletion that occurs near $k \approx N = 9$ for $x < 0$ as indicated by blue regions. Further, near the origin, penetration for $x > 0$ is discernible. Examining

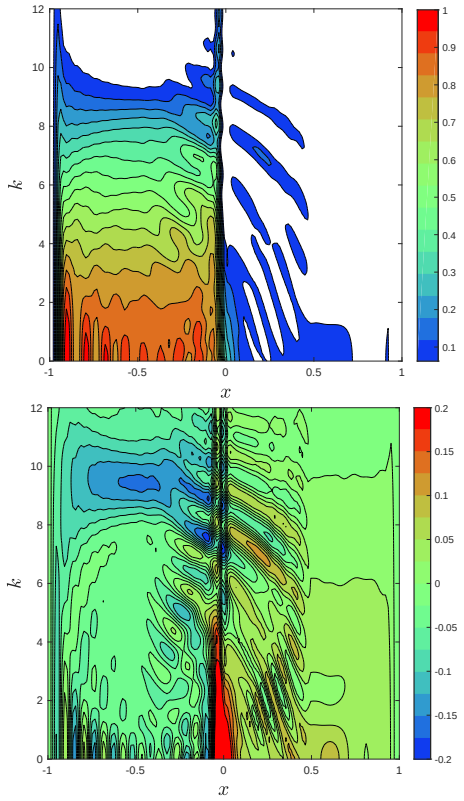

FIG. 9. Same as Figure 8 but for $n_f = 6$, $N = 9$, and $T = 300$ K. (*top*) $f(x,k)$ showing trajectories, with negative regions suppressed. Notice penetration into $x > 0$ region for small k; (*bottom*) $\Delta f(x,k) = f(x,k) - f_o(x,k)$, showing the more consequential changes that occur as a consequence of N near to n_f, with negative regions shown.

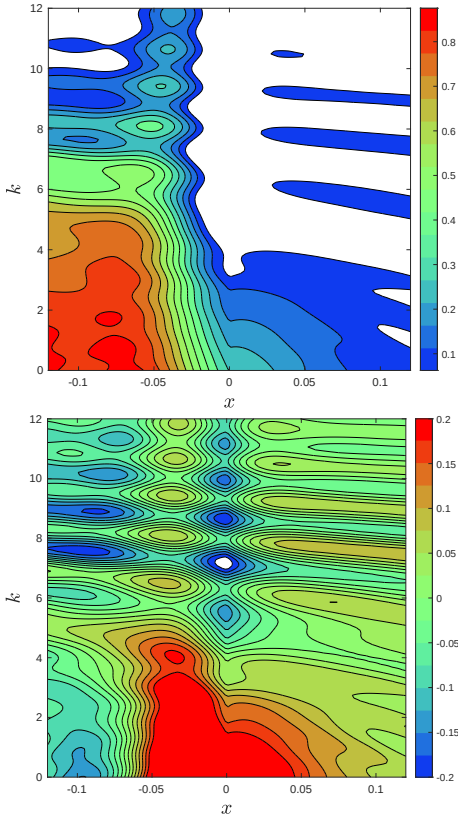

FIG. 10. Same as Figure 8 but for $n_f = 6$, $N = 9$, and $T = 300$ K. (*top*) $f(x,k)$ showing trajectories, with negative regions suppressed. Notice penegtration into $x > 0$ region for small k; (*bottom*) $\Delta f(x,k) = f(x,k) - f_o(x,k)$, showing the more consequential changes that occur as a consequence of N near to n_f, with negative regions shown.

the region near the origin, as in Figure 10, reveals trajectories associated with penetration of the barrier. Examining $f(x,k) - f_o(x,k)$ does not alter trajectories for $x > 0$, but does make more apparent where the trajectories originate for $x < 0$. In Figure 9, it is clear that for $k \approx k_o$, $f(x,k)$ is altered, and that for $x < 0$, the contours are associated with regions where $f(x,k)$ has diminished compared to $f_o(x,k)$ for $x < 0$.

The trajectories in phase space for a steady state distribution are contours, *e.g.*, the contour lines of $f(x,k)$ for the harmonic oscillator follow paths for which (in dimensionless coordinates) $x^2 + k^2 = \varepsilon$, where the "energy" ε is a constant[37,49,59] (see, however, Ref. 61 treating the parabolic tunneling barrier and Ref. 41 treating the double-well potential to illuminate distinctions between classical and Wigner trajectories). Behavior of the contour-trajectories for Wigner functions has been used to investigate tunneling delay and resonant tunneling effects[60,62] (compare to tunneling times inferred from time-dependent Gaussian wave packets evaluated using the Wigner function[63]). Here, the behavior of such trajectories are examined and assessed as to their utility in modeling a tunneling time for an analytically exact model. A first complication is immediately apparent for phase space points digitally extracted from contour lines and using average-velocity methods to extract time from them (Eq. (33) of Ref. 56). For some of the trajectories encountered here, such as the 0.125 line of Figure 10(a), the trajectory "folds back" so that even though the velocity k_i is positive, the next step $x_{i+1} < x_i$, and therefore the interpretation is divergent from what is meant by a classical trajectory: either a negative time step is obtained, or two forward trajectories originate from a vertex, with the "particle" associated with them perhaps jumping from a contour line elsewhere.

Seemingly better behaved trajectories obtained from using the same parameters as Figure 10 but taking the temperature to $T \to 0$ K are evident near the origin in Figure 11. Due to the symmetry $f(x,-k) = f(x,k)$, such trajectories are associated with a reflection of the "particle". To see the difficulty with a trajectory interpretation of these candidates, amend the previously used average-velocity approximation of $t_2 - t_1 \approx (\tilde{x}_2 - \tilde{x}_1)/\langle v(\tilde{x})\rangle$ to

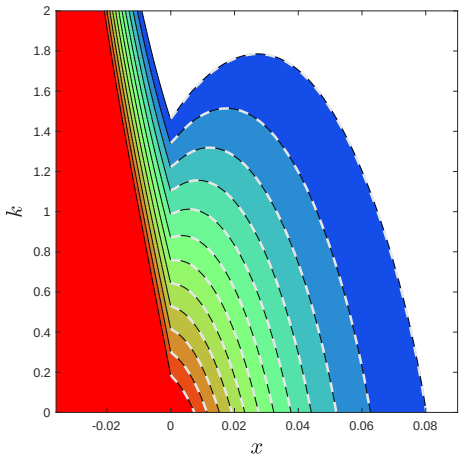

FIG. 11. Trajectories near origin for $n_f = 6$, $N = 9$, and $T = 0$ K. The trajectories penetrating into the split-well region ($x > 0$) are shown by dashed gray lines (12 in number). Lines (3,6,9,12) constitute the $x(t)$ trajectories of Figure 12.

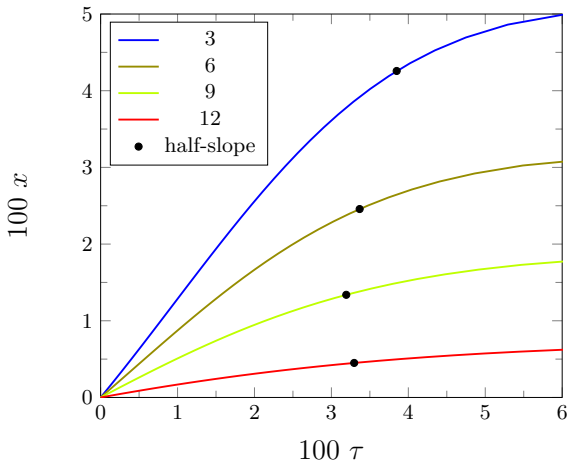

FIG. 12. $x(t)$ trajectories for dashed lines (3,6,9,12) of Figure 11. The black dots designated "half-slope" denote where the $dx/d\tau$ has fallen to half of its initial value.

properly account for velocity that is position-dependent. A time increment is properly obtained via

$$\Delta t = t_2 - t_1 = \int_{\tilde{x}_1}^{\tilde{x}_2} \frac{1}{v(x')} dx' \tag{51}$$

Thus, the average velocity approximation is valid only when $\langle 1/v(\tilde{x})\rangle \approx 1/\langle v(\tilde{x})\rangle$ with the tilde-notation denoting a dimensioned x. It is trivially shown that ballistic trajectories (those for which $v(\tilde{x})^2 + g\tilde{x} = 2\varepsilon/m$ for a constant acceleration g and energy ε) and harmonic oscillation trajectories (those for which $v(\tilde{x})^2 + a\tilde{x}^2 = 2\varepsilon/m$ for a spring constant a and energy ε) result in finite time increments when t_2 is the time at which the particle changes direction (the velocity changes sign). For the trajectories of Figure 11, however, it is seen that $k(x) \approx \alpha(x_2 - x)$ for a constant α such that $k(x_2) = 0$. As a result, the dimensionless time $\tau = 2\pi\hbar t/mL^2$ which is defined by

$$\tau(x) - \tau_1 = \int_{x_1}^{x} \frac{dx'}{k(x')} = \frac{1}{\alpha} \ln\left[\frac{x_2 - x_1}{x_2 - x}\right] \tag{52}$$

shows that $\Delta\tau = \tau_2 - \tau_1$ is logarithmically divergent as $x \to x_2$ where $k(x_2)$ crosses the axis and $x_1 = 0$. Converting that to a dimensioned time is accomplished by $\langle t_{1/2}\rangle = (mL^2/2\pi\hbar)\langle\tau_{1/2}\rangle$, which bears a similarity to the Büttiker-Landauer transversal time of $mL/\hbar\kappa$ in dimensioned coordinates, where $\hbar^2\kappa^2/2m = V_o - E$. Insofar as the Gamow factor $\theta = 2\sigma\kappa L$ is a measure of the depth of penetration in tunneling, where the dimensionless shape factor σ is dependent only on the relative geometry of the barrier[16,64], then the transversal time bears the same relation to $(mL^2/2\pi\hbar)$ that $\langle t_{1/2}\rangle$ exhibits, but shows an inverse square root divergence as $E \to V_o$ compared to the logarithmic divergence of the Wigner trajectories, behaviors that may be related to why that measure of transit is "disputed" (see Refs. 34 and 65 for discussions of the dispute).

A numerical evaluation of the tunneling time $\tau(x)$ by adding the increments $\Delta\tau_i = \tau_{i+1} - \tau_i$ over an array of numerically determined (x_i, k_i) values is thereby complicated by the logarithmic increase in $\Delta\tau_i$ as $k(x_i)$ approaches the x-axis. Nevertheless, a measure of the time scales involved are indicated in the behavior of τ_i in Figure 12, and in particular, the locations where $dx/d\tau$ has decreased to half of its initial value entering the barrier region at $x = 0$ (indicated by the black dots). Although there is spread in the half-values, their mean is $\langle\tau_{1/2}\rangle = 0.0343$. Some suggestive values allow for comparisons to magnitudes reported in the literature. For example, taking $L = 5$ nm, then $\langle t_{1/2}\rangle \approx 1.18$ fs, a duration comparable to photo assisted emission time estimates from sharpened tungsten emitters[53]. Alternately, if $\langle t_{1/2}\rangle$ is taken to be 0.05 fs (referred to as the *universal attosecond response to removal of an electron*[35]), then $L = 1$ nm, or comparable to the representative width of the image charge barrier in field emission to an electron at the Fermi level for which $L = F^{-1}\sqrt{\Phi^2 - 4QF}$,[59] where $Q = 0.36$ eV nm, $\Phi \approx 4.66$ eV for a typical metal, and a representative field is $q\mathcal{E} = F = 4$ eV/nm. Such comparisons, though, are speculative in the absence of an unambiguous referent for L. The sensitive dependence on the value of L and the energy levels E_j dependent upon it, and their relationship to $\langle t_{1/2}\rangle$ for field emission barriers, in which the constant V_o of the split well region is replaced by a linear field region, will be taken up in a future study: the time-dependent behavior of emission through a triangular barrier contains short time exotic structure[51] that anticipates intriguing features if an analogous Wigner model can be developed.

D. Excitation of Levels

Count rates of photoexcited electrons having absorbed one or more photons in intense laser fields[66–68] show structure that suggests cumulative three-step model processes (wherein electrons absorb photons, transport to the surface, and are emitted in a phenomenological model developed for photoemission[69,70], the concepts of which are applicable to secondary emission[71] as well) in which multiple photon absorptions induce plateaus. Modeling the transport after excitation with the three-step models implicitly use ballistic equations of motion for point-like particles in bulk, but the trajectory concept remains profitable as the electron leaves the surface[54]. As Kruger, *et al.* observe, however, electron position and momentum distributions for photoexcited electrons emerging over, or tunneling through, barriers modified by image charge forces and subject to surface fields are inherently ambiguous. If Wigner trajectories are to be useful in facilitating initial conditions of emitted electrons for particle-in-cell (PIC) codes, some features of the trajectory behavior would need to harken to particle concepts on which PIC is dependent. That is, trajectories that surmount (or tunnel through) the surface barrier would have to exhibit recognizable features on which such simulations depend, whether or not all ambiguities associated with the Wigner trajectories previously mentioned are themselves resolved. The final consideration regarding the utility of Wigner trajectories will therefore examine how trajectories are affected by excitations, wherein the occupation of one level is shifted to a higher level.

Excitation is represented by an electron in the j^{th} level absorbing a photon and subsequently occupying a higher level $E_j + \hbar\omega \to E_{j'}$. Although a single excitation is implied, the process can be thought of as multiphoton as well: for example, multiphoton absorption of otherwise long wavelength photons (infrared) can cumulatively elevate the electron energy to above the surface emission barrier for fs laser induced electron emission from tungsten needles coated with nanocrystalline diamond, where the nanocrystals are approximately 20 nm and the multiphoton absorption is sufficiently efficient[55]. Modeling the transition here is accomplished by transferring the occupation probability of the j^{th} level up to the j'^{th} level. The photon energy $\hbar\omega$ need not exactly equal $E_{j'} - E_j$ (although for convenience the model here assumes so): quantized levels are only along the axis normal to the surface, unless the range of the transverse coordinates are similarly constrained. Excess energy beyond that which enables the $j \to j'$ transition affects the mean transverse energy (MTE) of the emitted electrons, and though MTE has important consequences for emittance and beam brightness[10,72] in addition to surface roughness and other processes[12], the consequences of that contribution to MTE is deferred. Instead, the effects on the trajectories and their relation to excitation and passage over to the previously inaccessible split well region are examined exclusively.

Numerically, "excitation" is modeled by making the following alterations to an equilibrium distribution in which the occupation coefficients of Eqs. (8) and (9) are adjusted. Initially, f_j is occupied (> 0) and $f_{j'}$ is not (≈ 0). After excitation,

$$\begin{aligned} f_j &\to 0 \\ f_{j'} &\to f_j \frac{\Delta_j}{\Delta_{j'}} = f_j \left[\frac{k_{j+1} - k_{j-1}}{k_{j+h+1} - k_{j+h-1}} \right] \end{aligned} \tag{53}$$

where $k_{j+h}^2 = k_j^2 + (mL^2/2\pi^2\hbar^2)\hbar\omega$. Although h is integer, the final state levels are more complex, being given by $k_{j+h} = n_{j+h} + s_{j+h}$. h, then, is the change in index modeling the transition. Three behaviors are to be examined: (*i*) the behavior of excitations below the split well level, or $k_{j'} < N$, expected to show only changes to levels on the left ($x < 0$) side of the split well; (*ii*) the behavior of excitations on the left when $k_{j'} > N$, expected to show some reflection, and the behavior of the excited levels on the right hand side ($x > 0$), expected to show some change in level associated with a reduction in energy; and (*iii*) how temperature affects the excited trajectories.

The base-line condition is characterized by the parameters $n_f = N = 18$, and $T = 0$ K. Setting the Fermi level to the split well height is idiosyncratic, but chosen because that combination shows behavior that would be too small to be observed otherwise were there a larger difference. A larger value of n_f is chosen than before so as to enable the choice of a more interesting initial level. $f(x,k)$ is shown in Figure 13, and the difference $\Delta f(x,k) = f(x,k) - f_o(x,k)$ is shown adjacently to highlight where departures due to barrier penetration are most noticeable.

The first modification is to excite the $j = 13$ level with $k_j = 12.7495$ to the $j' = j + h = 18$ level with $k_{j'} = 17.5697$. Because of the subtleties associated with the spacing of the levels, $k_{j'} < N$: as a result, there is no visible contribution to probability for $x > 0$, but the appearance of a level (increased level at $j' = j + h$) associated with a reduction at j, on the left side ($x < 0$) is now clearly visible in Figure 14.

Increasing the excitation to $h = 15$ is next, so that $j' = j + h = 28$ with $k_{j'} = 19.7488$. If values fashioned after the aforementioned multiphoton absorption study of Tafel, *et al.* (Ref. 55) of $\lambda = 1392$ nm, $m_n = 0.57m$, but with $L = 10.3$ nm, are used (the Fermi level of $n_f = 18$ however is entirely *ad hoc*), then

$$\frac{2\pi^2\hbar^2}{m_n L^2}\left(k_{j'}^2 - k_j^2\right) \approx 5\hbar\omega$$

or five photons, (were $L = 23.1$ nm, then the transition would correspond to one photon). For $h = 18$, the contributions of temperature are discernible but not dramatic.

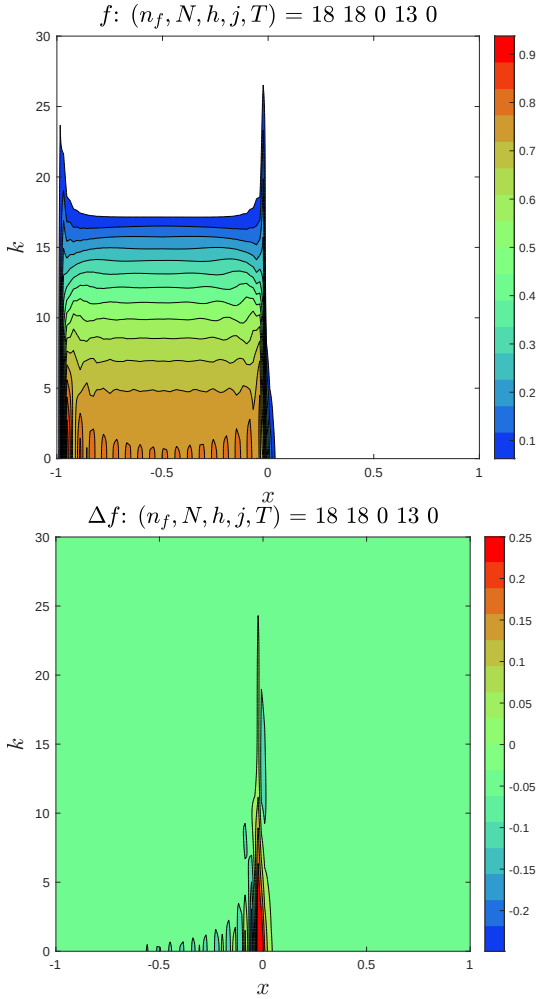

FIG. 13. Baseline $f(x,k)$ for study of photoexcitation. Parameters are $n_f = N = 18$ and $T = 0$ K. (*top*) $f(x,k)$; (*bottom*) $f(x,k) - f_o(x,k)$. The excitation level j is unused for the baseline configuration.

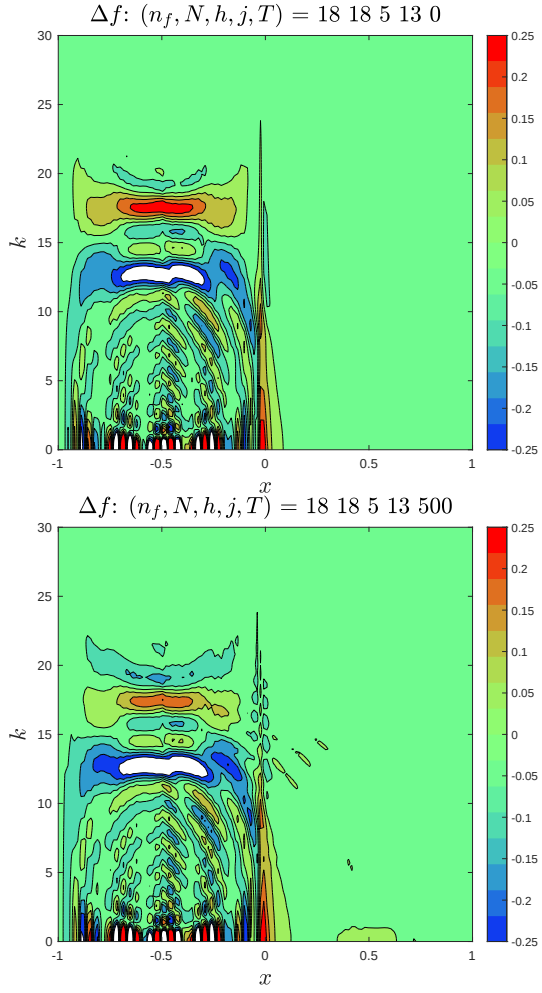

FIG. 14. Excitation of $j = 13$ by $h = 5$ (*top*) $T = 0$ K; (*bottom*) $T = 500$ K. At the higher temperature, a small increase is seen in the $x > 0$ region for small energy, commensurate with a small reduction of the excited (red) level for $x < 0$ and $k \approx 18$.

The hash of activity that appears between the $j + h$ and j levels, centered near $x = 0$, has a behavior that is reminiscent of the similar highly oscillatory behavior occuring between parting Gaussian wave packets that have interacted as in, for example, Figures (1) and (2) of Ref. 60 (behavior that is also reminiscent of a wave packet hitting a barrier as in Figure (2) of Ref. 73) and is referred to as *entanglement* by Weinbub and Ferry.

V. CONCLUSION

An analytical solution to the split well Wigner function has been carried out. Doing so required numerically finding the location of the eigenstates k_j. Although these states are close to the states of the infinite well for k_j sufficiently below or above $k_o = N$, numerous additional states (approximately $\sqrt{2N+1}$) arise when $k_j \approx N$. For steady state conditions, the trajectories are given by contours of $f(x,k)$. Evaluating the time taken for a tunneling trajectory characterized by small k to reverse curiously exhibits a logarithmic divergence. At higher k, the trajectories exhibit behavior that will be difficult to reconcile with a particle viewpoint. Nevertheless, although additional effort is required to bring out a correspondence of the trajectory approach with the particle picture favored by the simulation of ballistic particles subject to Newtonian forces as characteristic of PIC codes, it is clear that the demonstration of confinement, partial transmission, and account for the change of the energy of the level is respected by the Wigner trajectories. The program of unification with PIC is not without substantial challenges: although steady state conditions such as those considered here allow for trajectories to be deduced from contour lines, evaluating the force term for a trajectory in a time dependent problem[42], which in-

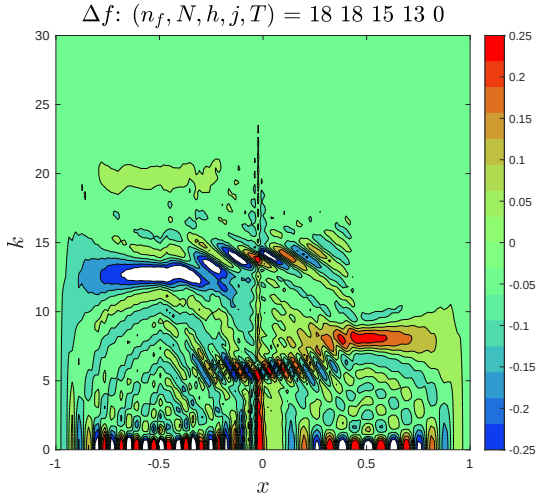

FIG. 15. Excitation of $j = 13$ by $h = 15$ at $T = 0$ K (higher temperatures are similar in overall behavior). Observe the state on the $x > 0$ of the right level h, but also a small reflected component at the location $j + h$ in the $x < 0$ region.

volves taking gradients of the Wigner function, may encounter difficulties due to the rapid oscillations apparent even in steady state, as in Figure 15. Smoothing the distribution as accomplished in the Husimi distribution[46] may offer respite, but at the cost of undermining the weighting of the trajectories in the evaluation of current. Therefore, although further development of the trajectory method for linking with particle-in-cell simulations is required, the development of an analytical and exact case as done here provides a means of assessing future numerical procedures that are likely to be required. By virtue of the split well configuration, an analytic $f(x, k)$ corresponding to tunneling completely through a barrier was not considered: such a circumstance will be reported separately.

ACKNOWLEDGMENTS

The authors gratefully acknowledge support by the Air Force Office of Scientific Research (AFOSR) through the lab task 18RDCOR016, Cathode Materials Research for High Power Microwave Sources. JLL was supported by AFOSR under the Award number FA9500-16-10037.

[1] J. R. Harris, K. L. Jensen, J. J. Petillo, S. Maestas, W. Tang, and D. A. Shiffler, J. Appl. Phys. **121**, 203303 (2017).
[2] J. R. Harris, IEEE Trans. Plas. Sci. **46**, 1872 (2018 June).
[3] W. Tang, D. Shiffler, K. Golby, M. LaCour, and T. Knowles, J. Vac. Sci. Technol. B **32**, 052202 (2014).
[4] W. Schottky, Zeitschrift für Physik **14**, 63 (1923).
[5] T. Stern, B. Gossling, and R. Fowler, Proc. R. Soc. A **124**, 699 (1929).
[6] R. Miller, Y. Lau, and J. Booske, J. Appl. Phys. **106**, 104903 (2009).
[7] J. R. Harris, K. L. Jensen, and D. A. Shiffler, J. Phys. D: Appl. Phys. **48**, 385203 (2015).
[8] K. L. Jensen, D. A. Shiffler, J. R. Harris, and J. J. Petillo, AIP Advances **6**, 065005 (2016).
[9] R. U. Martinelli, Appl. Opt. **12**, 1841 (1973).
[10] S. Karkare and I. V. Bazarov, Appl. Phys. Lett. **98**, 094104 (2011).
[11] D. H. Dowell, arXiv:1610.01242v3 (2016).
[12] K. L. Jensen, M. McDonald, O. Chubenko, D. A. Harris, John R. amd Shiffler, N. A. Moody, J. J. Petillo, and A. J. Jensen, Journal of Applied Physics **(in review)** (2019).
[13] K. Torfason, A. Valfells, and A. Manolescu, Phys. Plasmas **22**, 033109 (2015).
[14] A. Kyritsakis, G. Kokkorakis, J. Xanthakis, T. Kirk, and D. Pescia, Appl. Phys. Lett. **97**, 023104 (2010).
[15] A. Kyritsakis and J. P. Xanthakis, Proc. R. Soc. A **471**, 20140811 (2015).
[16] K. L. Jensen, D. A. Shiffler, M. Peckerar, J. R. Harris, and J. J. Petillo, J. Appl. Phys. **122**, 064501 (2017).
[17] V. T. Binh, S. T. Purcell, N. Garcia, and J. Doglioni, Phys. Rev. Lett. **69**, 2527 (1992).
[18] J. Shaw and J. Itoh, in *Vacuum Microelectronics*, edited by W. Zhu (Wiley, New York, 2001) p. 187.
[19] L. Gallmann, I. Jordan, H. J. Worner, L. Castiglioni, , M. Hengsberger, J. Osterwalder, C. A. Arrell, M. Chergui, , E. Liberatore, U. Rothlisberger, and U. Keller, Structural Dynamics **4** (2017).
[20] D. B. Go and D. A. Pohlman, J. Appl. Phys. **107**, 103303 (2010).
[21] J. P. Edelen, S. G. Biedron, J. R. Harris, S. V. Milton, and J. W. Lewellen, Phys. Rev. ST Accel. Beams **18** (2015).
[22] S. D. Dynako, A. M. Loveless, and A. L. Garner, Phys. Plasmas **25** (2018).
[23] A. Pedersen, A. Manolescu, and A. Valfells, Phys. Rev. Lett. **104**, 175002 (2010).
[24] P. Zhang, A. Valfells, L. K. Ang, J. W. Luginsland, and Y. Y. Lau, Applied Physics Reviews **4**, 011304 (2017).
[25] K. R. Spangenberg, *Vacuum Tubes* (McGraw-Hill, 1948).
[26] R. Forbes, Journal of Applied Physics **104**, 084303 (2008).
[27] A. Rokhlenko, K. L. Jensen, and J. L. Lebowitz, Journal of Applied Physics **107**, 014904 (2010).
[28] K. L. Jensen, D. A. Shiffler, I. M. Rittersdorf, J. L. Lebowitz, J. R. Harris, Y. Y. Lau, J. J. Petillo, W. Tang, and J. W. Luginsland, Journal of Applied Physics **117**, 194902 (2015).
[29] A. Valfells, D. W. Feldman, M. Virgo, P. G. O'Shea, and Y. Y. Lau, Physics of Plasmas **9**, 2377 (2002).
[30] L. K. Ang, W. S. Koh, Y. Y. Lau, and T. J. T. Kwan, Phys. Plasmas **13**, 056701 (2006).
[31] W. Koh and L. Ang, Appl. Phys. Lett. **89**, 183107 (2006).
[32] K. Nemeth, K. C. Harkay, M. van Veenendaal, , L. Spentzouris, M. White, K. Attenkofer, Srajer, and George, Phys. Rev. Lett. **104**, 046801 (2010).
[33] N. A. Moody, K. L. Jensen, A. Shabaev, S. G. Lambrakos, J. Smedley, D. Finkenstadt, J. M. Pietryga, P. M. Anisimov, V. Pavlenko, E. R. Batista, J. W. Lewellen, F. Liu, G. Gupta, A. Mohite, H. Yamaguchi, M. A. Hoffbauer, and I. Robel, Physical Review Applied **10**, 047002 (2018).
[34] E. H. Hauge and J. A. Støvneng, Rev. Mod. Phys. **61**, 917 (1989).
[35] A. S. Landsman and U. Keller, Phys. Rep. **547**, 1 (2015).
[36] T. Zimmermann, S. Mishra, B. R. Doran, Gordon, D. F., and A. S. Landsman, Phys. Rev. Lett. **116** (2016).
[37] M. Hillery, R. Oconnell, M. Scully, and E. Wigner, Phys. Rep. **106**, 121 (1984).
[38] M. Belloni, M. A. Doncheski, and R. W. Robinett, American Journal of Physics **72**, 1183 (2004).
[39] M. Belloni and R. Robinett, Phys. Rep. **540**, 25 (2014).
[40] F. A. Buot and K. L. Jensen, Phys. Rev. B **42**, 9429 (1990).
[41] M. Razavy, Phys. Lett. A **212**, 119 (1996).
[42] S. Dries, B. Fons, and M. Wim, Physica A: Statistical Mechanics and its Applications **391**, 78 (2012).
[43] F. A. Buot and A. K. Rajagopal, Superlattices Microstruct. **23**, 641 (1998).
[44] F. Martin, J. Garcia-Garcia, X. Oriols, and J. Sune, Jpn. J. Appl. Phys. **38**, 2669 (1999).

[45]X. Oriols, J. Garcia-Garcia, F. Martin, J. Sune, J. Mateos, T. Gonzalez, D. Pardo, and O. Vanbesien, Semiconductor Science and Technology **14**, 532 (1999).
[46]E. Colomés, Z. Zhan, and X. Oriols, Journal of Computational Electronics **14**, 894 (2015).
[47]R. H. Fowler and L. Nordheim, Proc. R. Soc. A **119**, 173 (1928).
[48]E. L. Murphy and R. H. Good, Phys. Rev. **102**, 1464 (1956).
[49]W. R. Frensley, Rev. Mod. Phys. **62**, 745 (1990).
[50]K. L. Jensen and A. Ganguly, J. Appl. Phys. **73**, 4409 (1993).
[51]O. Costin, R. Costin, I. Jauslin, and J. L. Lebowitz, J. Appl. Phys. **124** (2018).
[52]K. L. Jensen, J. J. Petillo, S. Ovtchinnikov, N. Panagos, Dimitrios, N. A. Moody, and S. G. Lambrakos, J. Appl. Phys. **122**, 164501 (2017).
[53]C. Kealhofer, S. M. Foreman, P. Hommelhoff, and M. A. Kasevich, Springer Series in Chemical Physics **92**, 702 (2009).
[54]M. Krüger, C. Lemell, G. Wachter, J. Burgd ́orfer, and P. Hommelhoff, J. Phys. B: At. Mol. Opt. **51**, 172001 (2018).
[55]A. Tafel, J. Ristein, and P. Hommelhoff, "Femtosecond laser-induced electron emission from nanodiamond-coated tungsten needle tips," arXiv:1903.05560 (2019).
[56]K. L. Jensen, D. A. Shiffler, J. L. Lebowitz, M. Cahay, and J. J. Petillo, J. Appl. Phys. **125**, 114303 (2019).
[57]M. Cahay and S. Bandyopadhyay, *Problems in Quantum Mechanics : For Material Scientists, Applied Physicists and Device Engineers* (John Wiley & Sons, Inc., Hoboken, New Jersey, 2017).
[58]R. Kubo, *Statistical Mechanics, an Advanced Course With Problems and Solutions* (North-Holland Pub. Co. Interscience Publishers, Amsterdam New York, 1965).
[59]K. L. Jensen, *Introduction to the Physics of Electron Emission* (John Wiley & Sons, Inc., Hoboken, New Jersey, 2017).
[60]J. Weinbub and D. K. Ferry, Applied Physics Reviews **5**, 041104 (2018).
[61]N. Balazs and A. Voros, Annals of Physics **199**, 123 (1990).
[62]Y. Hsu and G. Y. Wu, J. Appl. Phys. **71**, 304 (1992).
[63]N. Kluksdahl, A. Kriman, and D. Ferry, Superlattices Microstruct. **4**, 127 (1988).
[64]K. L. Jensen, Journal of Applied Physics **(submitted)** (2019).
[65]W. Truscott, Phys. Rev. Lett. , 1900 (1993).
[66]J. P. Girardeau-Montaut, C. Girardeau-Montaut, S. D. Moustaizis, and C. Fotakis, Appl. Phys. Lett. **64**, 3664 (1994).
[67]P. Hommelhoff, Y. Sortais, A. Aghajani-Talesh, and M. A. Kasevich, Phys. Rev. Lett. **96**, 077401 (2006).
[68]M. Schenk, M. Kr ́uger, and P. Hommelhoff, Phys. Rev. Lett. **105**, 257601 (2010).
[69]C. Berglund and W. Spicer, Phys. Rev. **136**, A1030 (1964).
[70]W. E. Spicer and A. Herrera-Gomez, Proc. SPIE Int. Soc. Opt. Eng. **2022**, 18 (1993).
[71]E. M. Baroody, Phys. Rev. **78**, 780 (1950).
[72]I. V. Bazarov, A. Kim, M. N. Lakshmanan, and J. M. Maxson, Phys. Rev. ST Accel. Beams **14**, 072001 (2011).
[73]C. Jacoboni and P. Bordone, Rep. Prog. Phys. **67**, 1033 (2004).